

PECVD low-permittivity organosilicate glass coatings: Adhesion, fracture and mechanical properties

Youbo Lin^a, Yong Xiang^a, Ting Y. Tsui^b, Joost J. Vlassak^{a,*}

^a School of Engineering and Applied Sciences, Harvard University, 29 Oxford Street, Cambridge, MA 02138, USA

^b Department of Chemical Engineering, Nanotechnology Institute, University of Waterloo, 200 University Avenue West, Waterloo, Ont., Canada N2L 3G1

Received 11 January 2008; received in revised form 19 April 2008; accepted 4 June 2008

Available online 3 July 2008

Abstract

The structure and mechanical behavior of organosilicate glass (OSG) coatings have been analyzed as a function of composition and UV irradiation time. A decrease in the OSG carbon content results in more networking bonds and increased connectivity; UV irradiation increases the connectivity by severing weak terminal bonds and stabilizes the network through local bond rearrangements. These structure modifications lead to a significant improvement in the stiffness, hardness, and fracture energy of these coatings. The networking bond density and mean connectivity number correlate well with the mechanical behavior of the OSG films, although network bond density weighted by bond energy is a more appropriate measure. The adhesion energy of silicon nitride to OSG is significantly higher than the cohesive energy of the OSG as a result of interface densification and crack-tip shielding. Subcritical fracture measurements in aqueous environments show that the detrimental effect of water on adhesion surpasses the effect of network connectivity.

© 2008 Acta Materialia Inc. Published by Elsevier Ltd. All rights reserved.

Keywords: Low-permittivity; Organosilicate glass; Thin film; Mechanical properties; Fracture

1. Introduction

As the microelectronics industry strives to manufacture high-performance integrated circuits at lower cost, new materials are introduced to meet the evermore-stringent requirements raised by the shrinking feature size. Dielectric materials with low permittivity, primarily organosilicate glass (OSG) fabricated with plasma-enhanced chemical vapor deposition (PECVD) technologies, are employed to replace conventional silicon dioxide as the inter-metal insulator. These new materials are necessary to reduce the interconnect delay and power dissipation associated with the capacitive coupling between closely placed copper wires. Fully dense OSG has a bulk dielectric constant that is tunable from 2.8 to 3.3, and is currently used in the production of advanced integrated circuits. However, to meet the requirements for future technology nodes, the dielectric

constant needs to be reduced even more and this requires the introduction of porosity into the OSG coatings [1].

The low dielectric permittivity of OSG as compared to silica is attributed primarily to its lower density, which results from the disruption of the silicon dioxide network by terminal organic groups (mostly methyl groups) [2,3]. Introduction of these organic groups lowers the dielectric constant k at the expense of the mechanical integrity of the material, making it a challenge to integrate these dielectrics without causing reliability issues such as delamination and cracking during or after manufacturing [4]. Hence it is important to optimize the mechanical properties of OSG coatings through a good understanding of the relationship between film matrix structure and mechanical behavior, especially if porous films are to be used [5].

In this study, we try to shed light on this relationship by measuring the mechanical response of a series of OSG films and by correlating this response with the network structure of the films. In a recent paper, we presented a systematic analysis of the composition, structure and

* Corresponding author.

E-mail address: vlassak@esag.harvard.edu (J.J. Vlassak).

polarization of a set of OSG films deposited using octamethylcyclotetrasiloxane (OMCTS) as a precursor [3]. Based on this analysis, a quantitative structure model for OSG was proposed and the densities of the various bonds in the OSG network were derived. Infrared (IR) absorption inverse cross-sections, which relate the peak area in an IR spectrum to the number density of the corresponding bond in the material, were determined for various groups. In this paper, we discuss results obtained for OSG films that were deposited using two different precursors. Films deposited using one of the precursors were grown under a wide range of precursor flow conditions. Films deposited using the other precursor were exposed to ultraviolet radiation for different periods of time. These OSG films provide information on the structure evolution of OSG via bond stabilization and cross-linking with little variation in composition and dielectric constant. The Fourier transform infrared (FTIR) spectra of the OSG films were analyzed utilizing infrared absorption inverse cross-sections [3]. Mechanical properties, such as stiffness, hardness, and cohesive and adhesive energies of the OSG films, were systematically measured and related to the structure of the films.

2. Experiment

OSG films were deposited on 200 mm (100) silicon wafers at 400 °C in an industrial PECVD system using OMCTS as a precursor. Helium and oxygen served as carrier gas and oxidizer, respectively. Four OSG films with different compositions (denoted by OSG-1, 2, 3, 4, respectively, and referred to as the OSG-series) were fabricated by varying the flow rate of the OMCTS precursor. The thickness of the OSG-series films was 1.5 μm , except for the films used in the fracture measurements, which were 0.5 μm thick. The dielectric constant of the OSG-series films varied from 3.08 to 3.33 as measured using a KLA Quantox XP metrology system. These OSG films were characterized as deposited; no post-deposition thermal anneal was performed. Another set of OSG films with thicknesses of 0.9 μm was deposited at 275 °C on 300 mm (100) silicon wafers using diethoxymethylsilane (DEMS) as a precursor. These films were subsequently cured in a single step using a commercial broadband UV-source for 0, 2, 10, 20, 30, and 40 min (denoted by UV-1, 2, 3, 4, 5, 6, respectively, and referred to as the UV-series films). This UV-curing process took place in ultra-high vacuum and at a temperature of 400 °C. The dielectric constants of the UV-cured films ranged from 2.90 to 2.98 while the dielectric constant of the uncured film (UV-1) was 3.15.

The structure of the OSG-series films was discussed in detail in a previous paper [3]. The structure of the UV-series films was characterized by means of FTIR spectroscopy. The measurements were made in transmission mode at a resolution of 2 cm^{-1} using a Nicolet NEXUS 670 spectrometer equipped with an MCT-A detector and a KBr beam splitter. The concentration of the various

bonding structures was determined using the infrared inverse cross-sections reported previously [3].

The stress–strain curves of the OSG-series films were measured by means of the plane-strain bulge test [6]. In this test, the stress–strain curve of a thin film is determined by deflecting membranes fabricated from the film of interest. As shown in Fig. 1a, freestanding composite membranes consisting of 80 nm LPCVD Si_3N_4 /1.5 μm OSG/30 nm PECVD Si_3N_4 were fabricated using Si micromachining techniques [7,8]. Long rectangular windows were opened in the LPCVD Si_3N_4 coating on the backside of the wafer using photolithography and reactive ion etching (RIE). The exposed Si substrate was etched using a potassium hydroxide-based solution to create freestanding OSG films sandwiched between LPCVD and PECVD Si_3N_4 coatings. Freestanding LPCVD/PECVD Si_3N_4 bilayers with identical layer thicknesses were also prepared to subtract the contribution of the Si_3N_4 coatings, as shown in Fig. 1a.

The stress–strain curves of the OSG films were determined from the experimental pressure–deflection curves of the membranes using the following analytical formulae [6,7]:

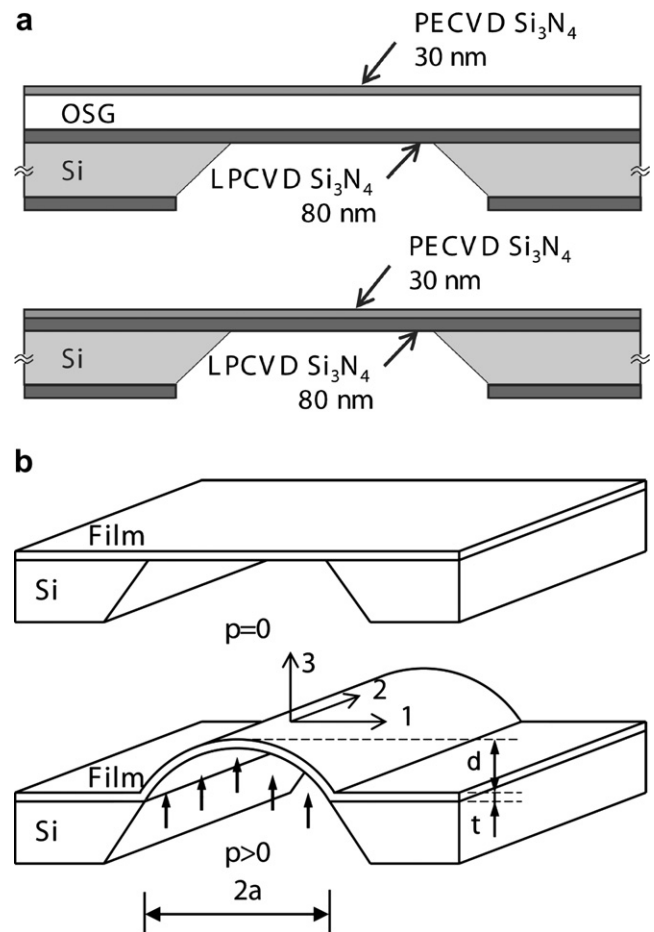


Fig. 1. Schematics of the bulge test specimens: (a) cross-sectional views of the freestanding OSG trilayers and Si_3N_4 bilayers; (b) perspective views of the specimen before and after pressurizing.

$$\sigma = \frac{p(a^2 + d^2)}{2td} \text{ and}$$

$$\varepsilon = \varepsilon_0 + \frac{a^2 + d^2}{2ad} \arcsin\left(\frac{2ad}{a^2 + d^2}\right) - 1 \quad (1)$$

where p is the applied pressure, d the membrane deflection, t the film thickness, $2a$ the membrane window width, as shown in Fig. 1b, and ε_0 the residual strain in the film. The strain rate was about 10^{-6} s^{-1} .

In addition to bulge tests, nanoindentation tests were performed on both the OSG- and the UV-series films using a MTS nanoindenter with a Berkovich indenter tip. The nanoindenter was operated in the continuous stiffness measurement mode with an oscillating load applied to the indenter tip [9,10]. This mode of operation allows the modulus and hardness to be determined continuously as a function of indentation depth. The indentation modulus, $M = E/(1 - \nu^2)$, and the hardness, H , were extracted from the experimental indentation curves using the following equations:

$$S = \beta \frac{2}{\sqrt{\pi}} M \sqrt{A} \text{ and } H = P/A \quad (2)$$

after correction for the finite compliance of the indenter tip and load frame. In these equations, P is the indentation load and A the projected contact area; E and ν are Young's modulus and Poisson's ratio of the material, respectively, and $\beta \approx 1.034$ is a correction factor for the Berkovich indenter [11]. The contact stiffness $S = dP/d\delta$ was obtained from the dynamic response of the indenter during the measurement. The projected contact area was calculated from the contact stiffness and the applied load as described by Oliver and Pharr [10].

The cohesive energy of the UV-4 and the OSG-series films was measured utilizing the double cantilever beam (DCB) technique [12], in which the OSG films were sandwiched between two silicon substrates and subjected to mode I loading as illustrated in Fig. 2a. The sample preparation and testing process is described below. The mode I loading forces a crack to propagate in the interior of the films, so that the cohesive fracture energies of the OSG films are measured. Fig. 2b shows a typical load–displacement curve. The load increases linearly under a constant displacement rate of $0.3 \mu\text{m s}^{-1}$ until it reaches a critical point at which the crack starts to grow and the load decreases. The load continues to drop with further crack extension. The specimen is then unloaded and reloaded several times during the process, to determine the crack length from the specimen compliance according to [12]:

$$c = \left(\frac{DEbh^3}{8P(1 - \nu^2)} \right)^{1/3} - 0.64h \quad (3)$$

where c is the crack length, D the displacement, b and h , the width and the half height of the beam, P the load, and E , ν the Young's modulus and Poisson's ratio of silicon. The corresponding energy release rate is given by [12]:

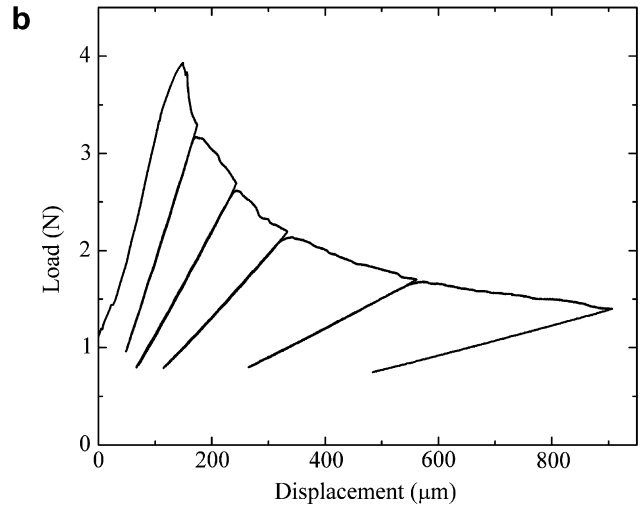
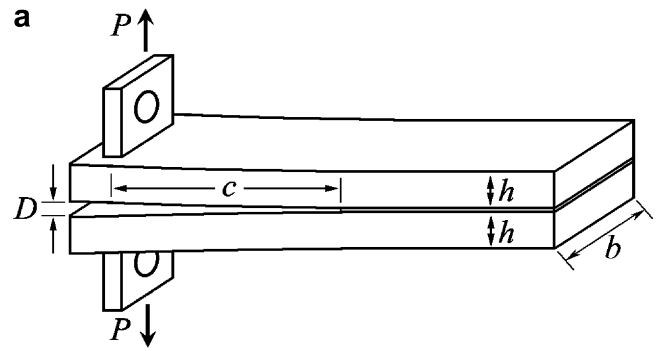


Fig. 2. (a) Schematic view of a DCB test specimen. (b) A typical load–displacement curve for the DCB tests.

$$G = \frac{12P^2c^2(1 - \nu^2)}{Eb^2h^3} \left(1 + 0.64 \frac{h}{c} \right)^2 \quad (4)$$

Finally, the adhesion energy of PECVD silicon nitride, which is a common barrier and etch stop layer in semiconductor processes, to the OSG-series films was characterized by means of the four-point bend (FPB) test [13,14]. A schematic view of the specimen geometry is shown in Fig. 3a. The film stack is sandwiched between two silicon substrates and a transverse notch is machined in one of the silicon substrates to facilitate crack initiation. This particular specimen and loading geometry applies almost equal amount of normal and shear stress to a crack in the plane of the film with a phase angle of approximately 43° . The mixed mode load drives the crack towards the OSG/silicon nitride interface. The corresponding energy release rate (or adhesion energy) is given by [13,14]:

$$G = \frac{21P^2l^2(1 - \nu^2)}{16Eb^2h^3} \quad (5)$$

When the interfacial crack is subject to a constant moment and its length is longer than the beam thickness, the energy release rate is independent of the crack length. A typical test curve is shown in Fig. 3b. In the linear loading region, a pre-crack emanates from the notch. The steps in the linear loading line occur when the pre-crack propagates in the

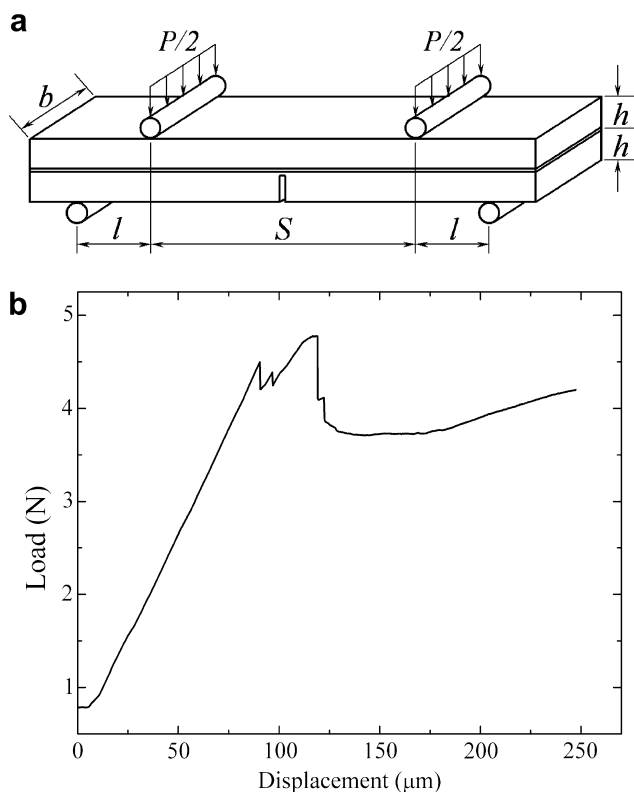


Fig. 3. (a) Schematic view of a FPB test specimen. (b) A typical load–displacement curve for the FPB test.

silicon substrate until it reaches the film stack. The interfacial crack is initiated when the applied load reaches a critical level. This process results in a steep drop in the load. Once the interfacial crack enters a steady state, a plateau is observed in the load–displacement curve. The adhesion energy is then calculated from the plateau load using Eq. (5). A standard displacement rate of $0.3 \mu\text{m s}^{-1}$ was maintained for all adhesion measurement in this study. It should be noted that the height of the plateau is a slight function of the displacement rate if there are reactive species in the environment [15]. In order to evaluate the effects of composition and structure on the susceptibility of OSG to stress-corrosion fracture, subcritical fracture measurements were performed on the OSG-series films in ambient and aqueous environments using the four-point bend test and a load–relaxation technique described previously [16–18].

Detailed sample preparation and testing procedures for the DCB and four-point bend experiments were reported previously [17,18]. Briefly, 500 nm thick OSG films were deposited on a silicon wafer. The films were exposed to an ammonia (NH_3) plasma and then capped by 100 nm PECVD silicon nitride. The wafers were then bonded to a blank silicon wafer with epoxy. The bonded wafers were cut into $65 \times 6 \text{ mm}^2$ (for FPB) or $65 \times 13 \text{ mm}^2$ (for DCB) pieces using a high-speed diamond dicing saw. For the FPB samples, a notch was made on the film-deposited substrate with the dicing saw to introduce a pre-crack, which propagates to the film stack during the test. For the DCB speci-

men, a razor blade was used to open a pre-crack at one end of the beam. All the DCB and FPB tests were performed at 26°C in dry N_2 .

After the DCB and FPB tests, the samples were opened and the fracture surfaces were identified using a Surface Science X-ray photoelectron spectroscopy (XPS) system, model SSX-100. Monoenergetic soft Al K_{α} X-rays (1486.6 eV) were used to irradiate the samples. The photoelectron take-off angle was 35° corresponding to a detection depth of $\sim 5 \text{ nm}$. An electron flood gun was used during the measurements to minimize charging of the sample surface. The binding energies were calibrated by setting the graphitic C 1s peak equal to 284.6 eV. Survey scans were made at a 150 eV pass energy and with a 1 mm spot size, while a 25 eV pass energy and a 0.3 mm spot size were used for high-resolution scans.

3. Results and discussion

3.1. Composition and structure

A systematic study of the composition and network structure of the OSG-series films was conducted previously [3]. Relevant results and conclusions are summarized here. As shown in Table 1, more carbon and less oxygen are incorporated into the film if the OMCTS flow rate is increased during the OSG deposition process. Both the mass density and the relative dielectric constant of the films decrease. FTIR analysis shows that carbon in the film takes the form of CH_3 and CH_2 , both of which substitute for oxygen in the network. As the carbon content increases the amount of CH_3 increases, while that of CH_2 decreases. Evidence obtained from the FTIR spectra further indicates that the film structure becomes less cross-linked with increasing carbon content [3]. This is exemplified in the change of the Si–O bond configurations, which show up as a broad band in the FTIR spectrum extending from 925 to 1250 cm^{-1} . Three configurations of Si–O bonds can be identified [19]: the network structure where one Si is connected to four O atoms (like in SiO_2) and the Si–O–Si bond angle is $\sim 144^\circ$, the caged structure where one of the O atoms is replaced by a terminal group and the Si–O–Si bond angle is larger than 144° , and the suboxide/chain structures where one or more O atoms are replaced and the Si–O–Si bond angle is less than 144° . The FTIR results show that the amount of network and caged structures decreases, while that of suboxide/chain structures increases with increasing OMCTS flow rate.

The bonds in the OSG network can be divided into two groups: terminal bonds and networking bonds. The former group includes Si– CH_3 , Si–H and Si–OH, while the latter includes Si–O and Si– CH_2 . The FTIR results indicate that the number of OH-groups in the OSG-series films is insignificant [3]. Consequently, hydroxyl groups are not included in the current analysis. The ratio of the Si– CH_3 /Si–O peak areas in the FTIR spectrum has been used as a parameter to characterize the OSG film structure

Table 1
Physical properties and structure of OSG-series films

Films	α -Silica	OSG-1	OSG-2	OSG-3	OSG-4
OMCTS flow rate (ff_i)		1.00	1.13	1.25	1.42
Relative dielectric constant, k	4.0	3.33 ± 0.17	3.22 ± 0.16	3.16 ± 0.16	3.08 ± 0.15
C/Si atomic ratio	0	0.68 ± 0.03	0.71 ± 0.04	0.75 ± 0.04	0.79 ± 0.04
Density (g cm^{-3})	2.25	1.525 ± 0.019	1.475 ± 0.017	1.446 ± 0.014	1.403 ± 0.017
Terminal ^a /networking bond ^b ratio	0	0.253 ± 0.055	0.268 ± 0.055	0.285 ± 0.058	0.307 ± 0.063
Networking bond density (10^{19} m^{-2})	2.01	1.535 ± 0.096	1.486 ± 0.095	1.434 ± 0.093	1.396 ± 0.091
Mean connectivity number $\langle r \rangle$	2.667	2.490 ± 0.164	2.478 ± 0.164	2.463 ± 0.163	2.446 ± 0.163
Weighted network bond density (10^{19} m^{-2})	2.01	1.361 ± 0.068	1.324 ± 0.066	1.289 ± 0.064	1.263 ± 0.063

^a Terminal bonds include Si–CH₃ and Si–H.

^b Networking bonds include Si–O and Si–CH₂.

and properties. A more accurate method would be to compare the number of all the terminal bonds to the number of all the networking bonds across the films. This comparison cannot be accomplished by simply combining the peak areas for the various bonds in the OSG, because infrared inverse cross-sections vary from peak to peak. If the infrared inverse cross-sections are known, however, it is possible to correlate the mechanical behavior directly with the various bonds densities in the OSG network. The infrared inverse cross-sections for OSG were determined in a previous paper [3]; the corresponding network bond densities and the terminal/networking bond ratios are listed in Table 1 for each of the OSG-series films.

The behavior of amorphous solids with a covalent network structure has been modeled using constraint theory [20–22]. In a continuous random network, each atom is bound to its nearest neighbors through short-range covalent bonds. Thus each atom is subject to constraints associated with bond stretching and bond bending. The mean connectivity number $\langle r \rangle$ is then defined as the average coordination number (CN) of the atoms in the network. For a binary system A_xB_{1-x} , for instance, $\langle r \rangle = x \cdot \text{CN}_A + (1-x) \cdot \text{CN}_B$. The connectivity number $\langle r \rangle$ has an impact on a number of materials properties [23–26]. From a mechanical point of view, it correlates with the rigidity of the network as it is a measure of the average number of constraints on each atom. Rigidity percolation occurs when $\langle r \rangle$ exceeds 2.4, at which point the system changes from under-constrained to over-constrained. Therefore, it seems logical to examine the correlation between the mean connectivity number and the mechanical behavior of the OSG films. Table 1 lists the mean connectivity numbers for the OSG-series films, as determined from the FTIR spectra using the inverse cross-sections from Ref. [3]. In the calculation, CH₃ and CH₂ groups were each counted as one “atom” with a coordination number of 1 and 2, respectively.

3.2. Stiffness and hardness

Typical bulge test pressure–deflection curves for the sandwiched films and the Si₃N₄ bilayers are presented in Fig. 4a. The corresponding stress–strain curves for the OSG series

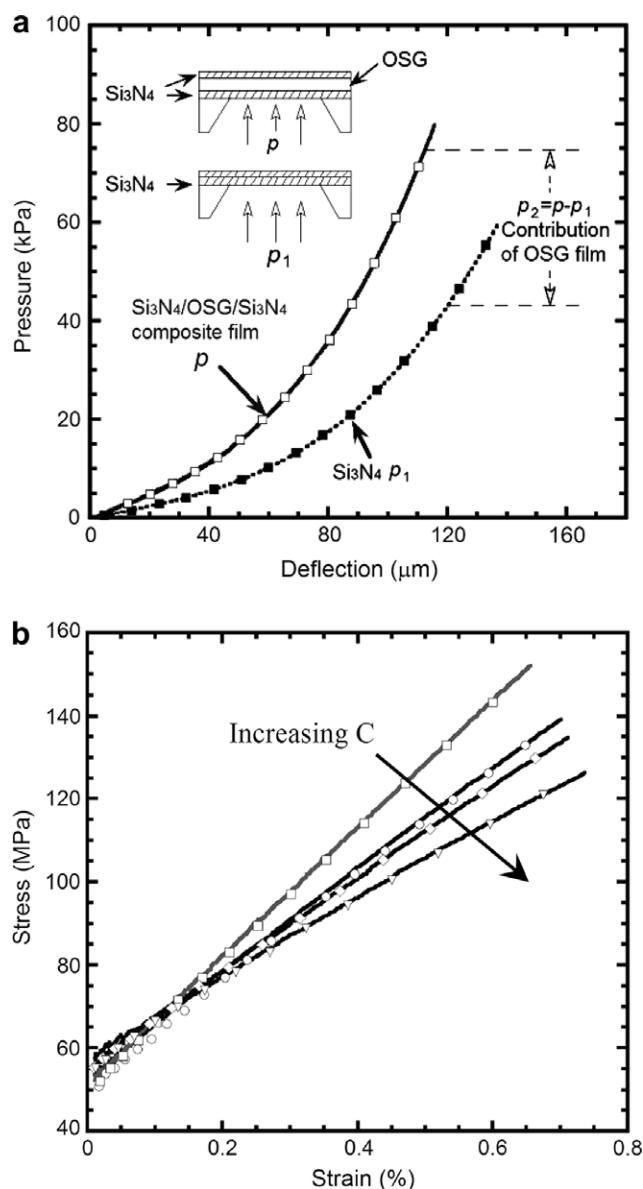


Fig. 4. (a) Typical pressure–deflection curves for sandwiched OSG films and Si₃N₄ bilayers. Each curve consists of loading (solid line for the composite films and dotted line for Si₃N₄ bilayers) and unloading (\square for OSG-1 and \blacksquare for Si₃N₄ bilayers) segments. (b) Plane-strain stress–strain curves of the OSG-series films obtained by subtracting the elastic contribution of the Si₃N₄ bilayers.

Table 2
Mechanical properties of OSG-series films

Films	Nanoindentation			Bulge test		
	Modulus* (GPa)	Fitted modulus (GPa)	Hardness* (GPa)	Plane strain modulus (GPa)	Residual stress (MPa)	Residual strain (10^{-3})
OSG-1	18.3 ± 0.9	15.6 ± 0.8	2.7 ± 0.1	15.9 ± 0.8	51.6 ± 2.6	3.4 ± 0.1
OSG-2	15.6 ± 0.8	13.3 ± 0.7	2.3 ± 0.1	13.5 ± 0.6	54.1 ± 2.6	4.2 ± 0.1
OSG-3	12.4 ± 0.7	10.4 ± 0.5	1.9 ± 0.1	11.3 ± 0.6	56.4 ± 2.8	5.0 ± 0.2
OSG-4	10.3 ± 0.6	9.2 ± 0.5	1.5 ± 0.1	9.5 ± 0.5	58.9 ± 2.9	6.4 ± 0.2
α -Silica	75.0 ± 0.8		10.2 ± 0.2			

* 5% rule.

films are presented in Fig. 4b. It is evident from the stress–strain curves that the films deform elastically; there is no sign of plastic deformation. The plain-strain moduli of the films were determined through linear regression of the stress–strain curves and are listed in Table 2. Clearly, the film stiffness decreases with increasing OMCTS flow rate.

The indentation modulus and hardness are presented as a function of normalized indentation depth δ/t in Fig. 5.

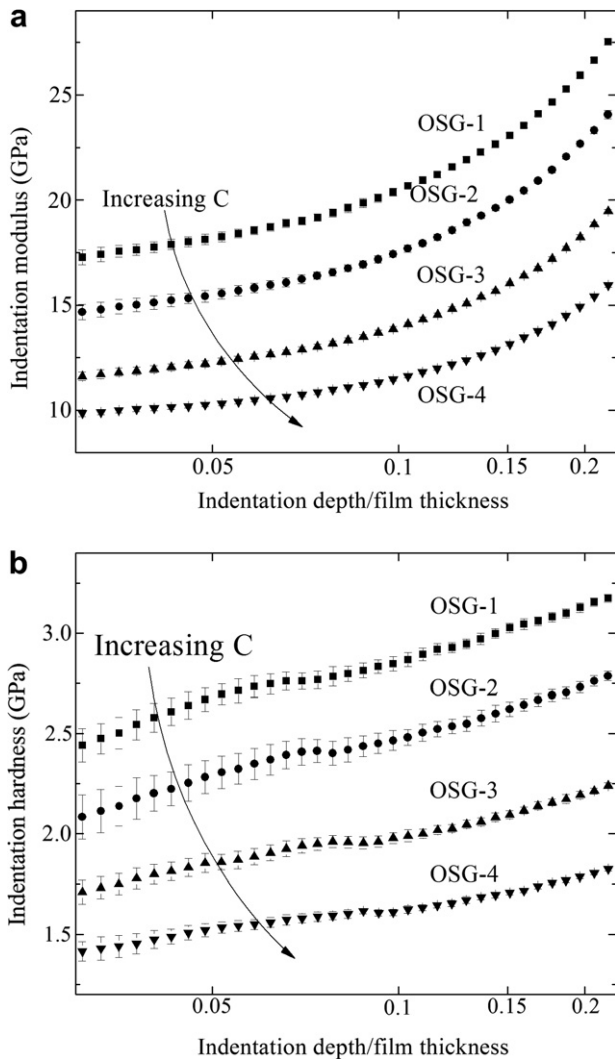


Fig. 5. (a) Indentation modulus and (b) hardness as a function of normalized indentation depth for the OSG-series films.

The increase in both properties with increasing indentation depth is due to the presence of the silicon substrate, a well-known phenomenon [27]. To minimize the impact of the substrate on the measurements, the indentation modulus and hardness of a coating are usually reported at indentation depths of less than 10% of the film thickness. Table 2 lists the modulus and hardness values obtained at a relative indentation depth of 5%. As expected, both modulus and hardness decrease with increasing OMCTS flow rate. For an isotropic material the indentation modulus is equal to the plane-strain modulus, i.e., the plane-strain modulus obtained from the bulge test can be directly compared with the indentation modulus. As is evident from Table 2, the indentation moduli are approximately 10–15% higher than the plane-strain moduli. We attribute this difference to the presence of the much stiffer silicon substrate. Much better agreement with the bulge test results is obtained if the indentation moduli are determined through linear extrapolation to zero indentation depth as illustrated in Fig. 6 (fitted modulus in Table 2).

The stiffness and hardness of the OSG-series films are comparable to or greater than those of other PECVD OSG films with similar dielectric constants [28–31], and superior to the same properties for spin-on glass [32–35]. This observation may be attributed to the energetic process

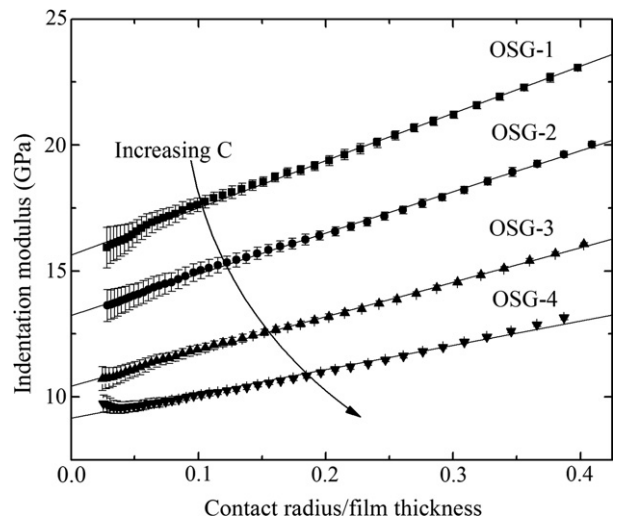


Fig. 6. Indentation modulus as a function of normalized contact radius for the OSG-series films. Solid lines are linear regression curves.

in PECVD, which preferentially sever weak bonds like Si–H and C–H in the precursor while preserving the siloxane backbone and thus promote cross-linking. A slight decrease in the carbon content of the OSG-series films results in only a modest increase in the dielectric constant, mean connectivity, and network bond density, but improves the stiffness and hardness by nearly 80%. This is achieved for the most part through increased bond cross-linking of the OSG network. The mechanical properties of OSG films are evidently very sensitive to the precise network structure of the films.

Next, we correlate the mechanical behavior of the OSG-series films with parameters describing the network structure. The stiffness and hardness are plotted as functions of the networking bond density in Fig. 7a and the mean connectivity number in Fig. 7b. All films have a mean con-

nectivity number $\langle r \rangle$ larger than 2.4, the rigidity percolation threshold. It has been reported that the addition of terminal nodes to an over-constrained covalent network, results in a softening of the material. The mechanical properties of such a network closely correlate with the mean connectivity number [23,36]. This is indeed borne out in Fig. 7b, where both stiffness and hardness correlate well with the mean connectivity number over the range of process parameters considered in this study. It should be noted, however, that network bond density provides an equally good description.

3.3. Effect of UV irradiation on film structure and mechanical properties

Fig. 8 shows the evolution of various bonds in the UV-series films as a function of UV irradiation time. Film properties and information obtained from the FTIR analysis are listed in Table 3. The mass densities obtained from the FTIR analysis are within 4% of the gravimetrically measured values. The as-deposited film (UV-1) has a larger density than most of the UV-irradiated films. The initial reduction in density upon irradiation suggests that there are entrapped volatile species that are removed from the network during irradiation process. This observation is supported by the FTIR results. For instance, Fig. 8a shows that the content of hydrocarbon species decreases with increasing irradiation time. These species may be methyl and methylene groups or other small hydrocarbon molecules that are weakly bound and entrapped in the network during film deposition and that gain enough energy to escape during UV irradiation. Most of the decrease in density occurs within the first 10 min of the irradiation process, indicating that the volatile hydrocarbon species are rapidly exhausted. With continuing UV irradiation, the disruption of Si- and O-bound methyl and methylene groups promote the formation of siloxane bond as shown in Fig. 8a. Fig. 8b illustrates that with increasing irradiation time, the number of methyl groups that are bound to Si decreases, while that of silicon-linked methylene increases. This observation suggests that UV irradiation converts some of methyl groups into methylene groups possibly by severing one of the C–H bonds and by the subsequent formation of a C–Si bond. Comparing the initial C–H bond density in Fig. 8a and b further suggests that there are indeed hydrocarbon species that are not bound to silicon. The amount of Si–H bonds is insignificant as shown in Fig. 8b. In Fig. 8c, we show the change of the different Si–O bond configurations during UV irradiation. Evidently, in addition to a net increase in the total number of bonds, the Si–O bonds are also reconfigured during the irradiation process. The unstable and energetically unfavorable cage/large angle Si–O bonds are converted to a silica-like network or the more stable suboxide [19,30].

Overall, UV irradiation removes the entrapped volatile species and disrupts the weak terminal groups in the film. It also supplies the energy for local bond rearrangements.

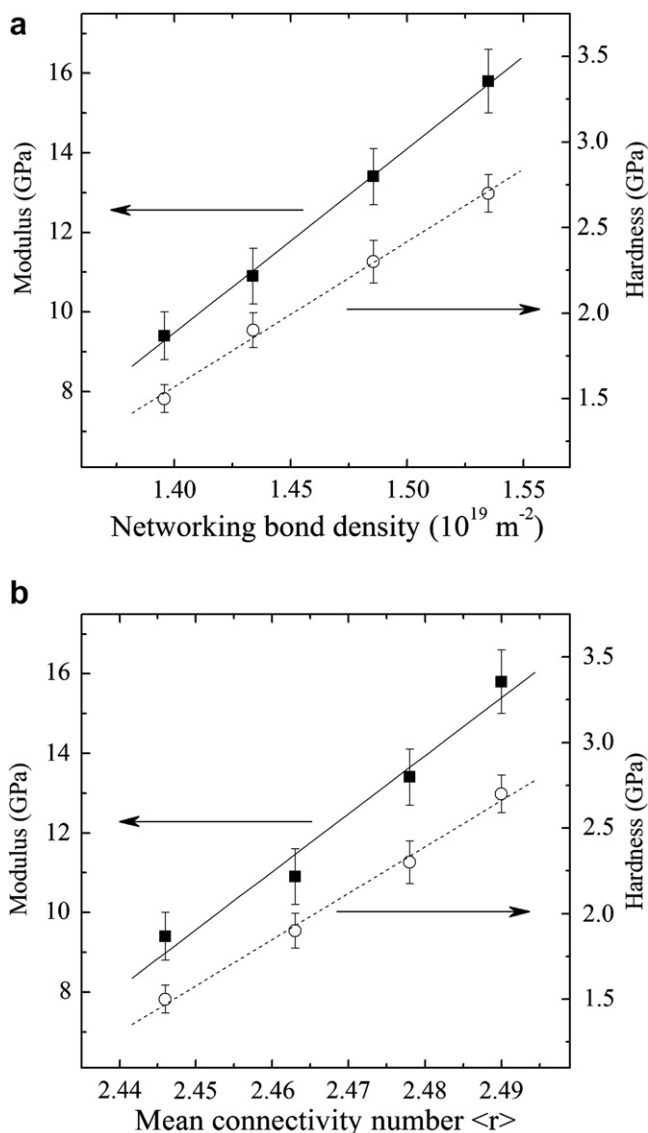


Fig. 7. Modulus and hardness of the OSG-series films presented as a function of: (a) the networking bond density and (b) the mean connectivity number. The modulus is an average of the values obtained from the bulge test and the indentation experiments.

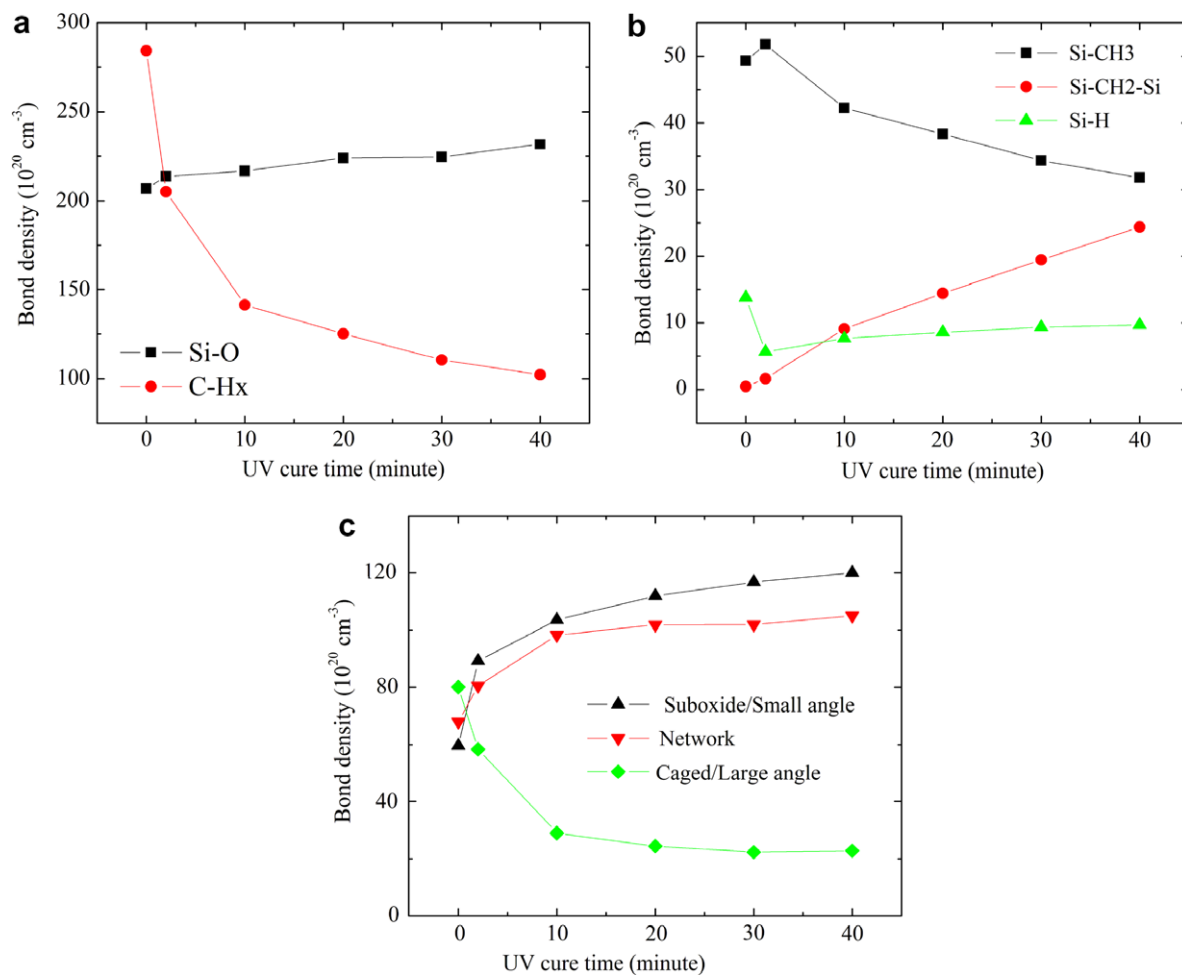


Fig. 8. Structure of OSG films with different UV cure time. (a) The concentration of siloxane bonds (based on the band at $1250\text{--}950 \text{ cm}^{-1}$) and hydrocarbon species (based on the band at $3010\text{--}2820 \text{ cm}^{-1}$ including CH_3 and CH_2). (b) The silicon-bound methyl (1274 cm^{-1}), methylene (1360 cm^{-1}), and Si–H bonds ($2320\text{--}2120 \text{ cm}^{-1}$). (c) Different forms of siloxane bonds shown in the broad band around $1250\text{--}950 \text{ cm}^{-1}$.

Table 3
Structure, physical and mechanical properties of UV-series films

Films	UV-1	UV-2	UV-3	UV-4	UV-5	UV-6
Cure time (min)	0	2	10	20	30	40
Dielectric constant k	3.15	2.90	2.91	2.93	2.96	2.98
Density (g cm^{-3})	1.473	1.375	1.431	1.468	1.458	1.503
Thickness reduction (%)		3.1	7.2	9.6	10.9	12.3
Modulus [#] (GPa)	7.3 ± 0.1	9.1 ± 0.1	13.3 ± 0.2	16.1 ± 0.3	19.1 ± 0.2	21.0 ± 0.3
Hardness* (GPa)	1.17 ± 0.05	1.52 ± 0.05	2.16 ± 0.07	2.53 ± 0.08	2.89 ± 0.08	3.06 ± 0.09
Mean connectivity number $\langle r \rangle$	2.451	2.473	2.501	2.516	2.528	2.540
Networking bond density (10^{19} m^{-2})	1.218	1.270	1.383	1.463	1.511	1.578
Weighted network bond density (10^{19} m^{-2})	1.208	1.249	1.318	1.375	1.403	1.452

[#] Fitted.

* 5% rule.

Thus it stabilizes the structure and promotes cross-linking in the network. In terms of its mechanical response, the film becomes more robust as evidenced by the increase in modulus and hardness values shown in Table 3. While the mechanical properties of the film increases significantly with irradiation, the value of the dielectric constant increases only slightly from 2.90 to 2.98. These results dem-

onstrate that, when optimized, the UV-cure process can greatly enhance the mechanical properties without significant reduction in electrical properties.

In Fig. 9a and b, the stiffness and hardness of the UV-series films are plotted against networking bond density and compared to those of the OSG-series films. The modulus values of the OSG-series are the same as shown in Fig.

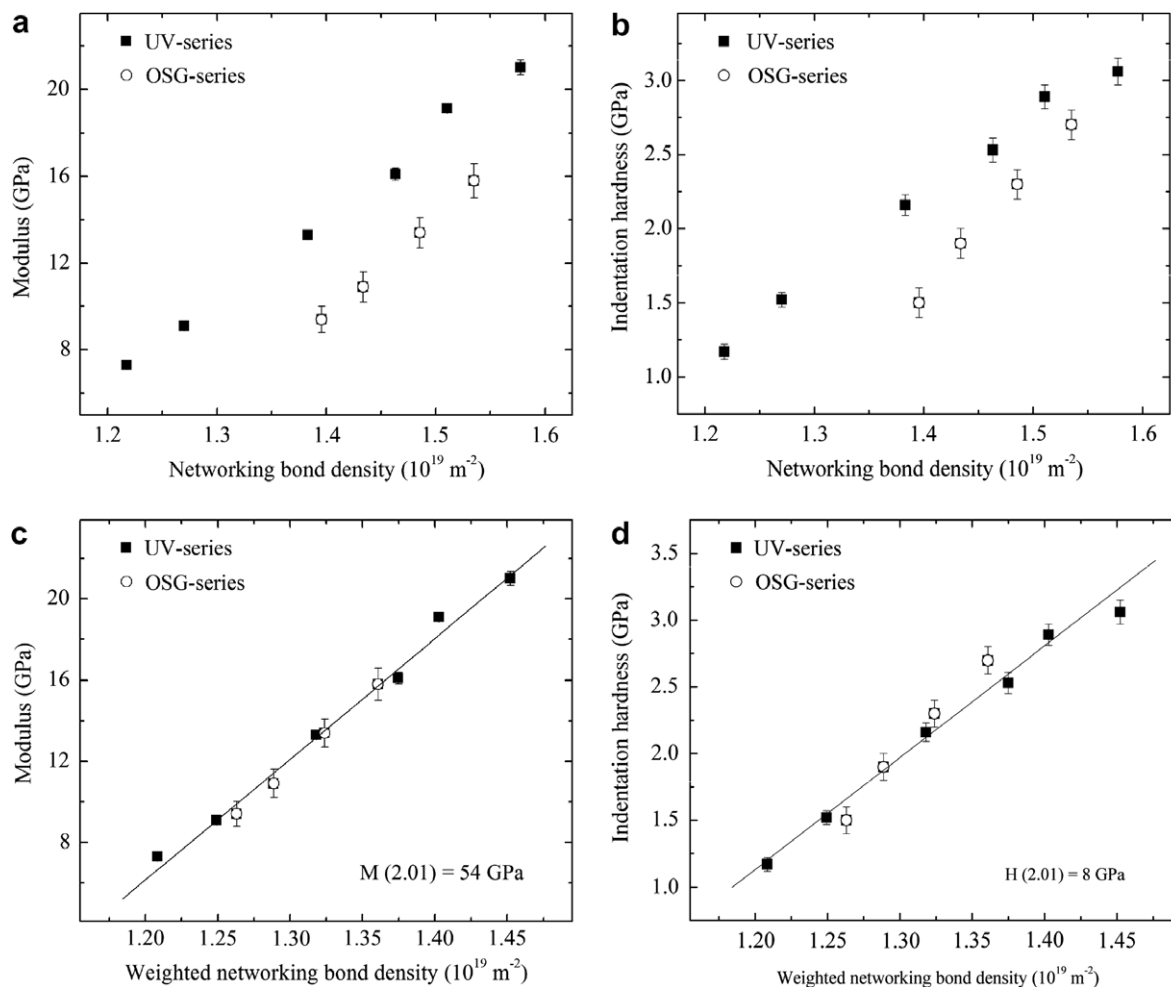


Fig. 9. Modulus (a) and hardness (b) of the UV- and OSG-series films plotted against networking bond density. The modulus (c) and hardness (d) are better described for both the UV- and OSG-series films if the networking bond density is weighted by the corresponding bond energies.

7; those of the UV-series are extrapolated from the indentation curves as described in the previous section. While both stiffness and hardness values correlate well with the network bond density, the data for UV- and OSG-series do not collapse, i.e., the network bond density alone does not suffice as a descriptor of the network structure. This is so because the Si–O and Si–CH₂ bonds are counted equally when calculating the network bond density, ignoring the fact that their respective bond stiffness and strength are quite different (800 kJ mol⁻¹ for Si–O versus 451 kJ mol⁻¹ for Si–C) [37]. Similarly, the mean connectivity number $\langle r \rangle$ fails to account for the different stiffness of the various bonds; thus $\langle r \rangle$ is not sufficient to describe the structure evolution either. An alternative approach is to weigh the densities of the various bonds by their respective bond energies. For instance, if a Si–O bond is counted as one, a Si–CH₂ bond counts for only 451/800, thus taking into account the reduced stiffness of the Si–CH₂ bond. We refer to the bond density calculated using this method as the weighted network bond density. Fig. 9c and d depict the stiffness and hardness of both the UV- and OSG-series films as a function of the weighted networking bond den-

sity. Evidently, the weighted networking bond density correlates very well with the mechanical properties of the OSG films over a wide range of process conditions and even works for OSG films deposited using different precursors.

3.4. Cohesive and adhesive fracture energies

The fracture energies, G_{IC} , of the OSG-series films and the UV-4 film as measured by the DCB test are listed in Table 4. XPS measurements (spectra not shown) indicate that fracture always takes place inside the OSG films. The adhesion energies of the PECVD Si₃N₄ barrier layers to the OSG-series films as measured by the FPB test are also listed in Table 4. Fig. 10a shows typical XPS survey spectra obtained from the crack faces. On the Si₃N₄ side, a strong N 1s signal is clearly identified; on the OSG side, no nitrogen signal is evident. This result would seem to indicate a clean interfacial fracture along the OSG/Si₃N₄ interface. High-resolution scans on the OSG side (Fig. 10b), however, reveal a small peak at 398.9 eV. This peak is associated with SiO–N bonds [38,39] that form when the OSG films are exposed to the ammonia plasma during

Table 4
Fracture and adhesion energies

Films	Fracture toughness, G_{IC} ($J m^{-2}$)	Adhesion energy to Si_3N_4 ($J m^{-2}$)
OSG-1	3.77 ± 0.56	6.89 ± 0.71
OSG-2	3.56 ± 0.26	6.16 ± 0.32
OSG-3	3.41 ± 0.20	5.84 ± 0.50
OSG-4	3.26 ± 0.21	4.58 ± 0.21
UV-4	3.73 ± 0.40	

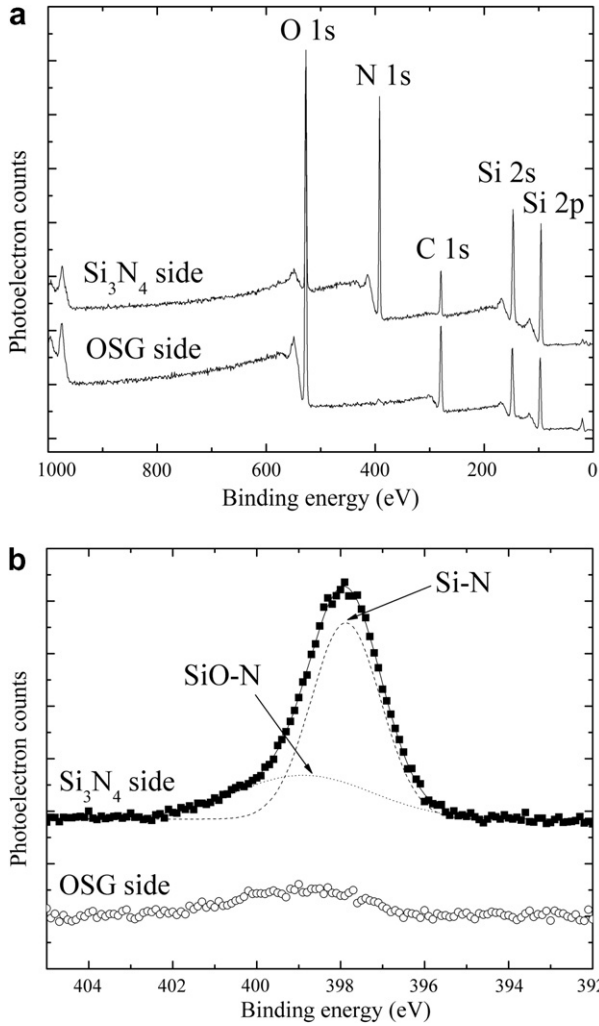


Fig. 10. (a) Survey scans of fracture surfaces showing the N 1s signal on the nitride side; (b) high-resolution spectra of the N 1s peak show SiO–N species on both sides.

the silicon nitride deposition process. The high-resolution N 1s peak obtained on the Si_3N_4 side (Fig. 10b) shows a shoulder on the high-energy side and actually consists of two peaks: A strong peak at 397.9 eV, which is due to the silicon nitride [40], and a weak peak at 398.9 eV, which corresponds to the same SiO–N bonds found on the OSG side. Thus it seems likely that a small amount of OSG material remains on the silicon nitride after fracture.

The adhesion energy and cohesive energy are plotted against the weighted network bond density in Fig. 11.

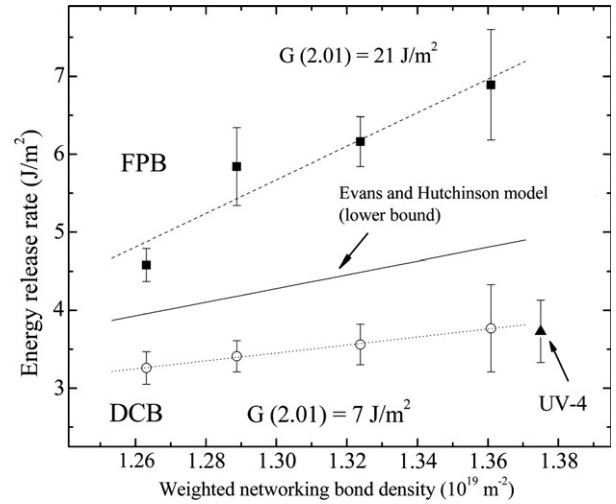


Fig. 11. Adhesion and cohesive fracture energy of the OSG-series films as a function of weighted networking bond density.

The cohesive energy scales linearly with the bond density and extrapolates to approximately $7 J m^{-2}$ for the weighted network bond density of fused silica, which is in reasonable agreement with the literature value of $7.6 J m^{-2}$ [41]. It is somewhat surprising, however, that the adhesive values are much larger than the cohesive energies. In order to explain this result, at least two factors need to be considered.

First, the loading mode is different between the two techniques (mixed mode in FPB vs. pure mode I in DCB). The effect of mode mixity on the fracture energy can be estimated from a model by Evans and Hutchinson [42]. This model examines shielding of the crack tip caused by contact between two non-planar crack faces. The phenomenon is governed by a parameter α_0 , which is a function of the material properties and the roughness of the crack faces:

$$\alpha_0 = 0.28MF^2/G_{IC}L \quad (6)$$

where F is the height of the steps on the crack surface and L the wavelength. These parameters may be determined by scanning the crack surfaces with an atomic force microscope. For the OSG-series films in this study, F and L were approximately 2 and 20 nm, respectively, yielding α_0 values from 0.23 to 0.16. Based on the fracture energies measured in the DCB experiments, the model predicts that the fracture energies obtained from the four-point measurement should follow the solid line in Fig. 11.

Second, the fracture location is different: in the FPB test, fracture occurs at the OSG/nitride interface and involves the topmost layer of the OSG film, while in the DCB test fracture occurs in the bulk of the film. This distinction is important because the OSG network bond density near the interface is higher than in the bulk of the film as a result of the exposure to the ammonia plasma during the deposition of the Si_3N_4 film. The densification caused by this plasma leads to a higher fracture energy for the interface.

As the values of M and G_{IC} that were used to estimate the contribution of crack-tip shielding from Eq. (6) are those for the interior of the OSG films and not for the densified interface, the solid line in Fig. 11 actually represents a lower bound for the effect of crack-tip shielding in the FPB test. Interface densification tends to further increase this effect and if the topmost layer of the OSG were fully densified with the same stiffness and cohesive energy as silica, the crack-tip shielding model would predict a fracture energy of approximately 11 J m^{-2} for the FPB measurements. Thus it is evident from Fig. 11 that both crack-tip shielding and interface densification contribute to the higher fracture energies obtained in the FPB measurements.

3.5. Subcritical fracture behavior

Fig. 12 depicts the velocity of cracks propagating at the OSG/silicon nitride interface as a function of applied energy release rate for OSG-series films in a dry environment ($\sim 10\%$ relative humidity) and in de-ionized water (pH 6.5). The curve for OSG-1 tested in the dry environment shows a well-defined plateau where the fracture process is limited by transport of water molecules to the crack tip. Projected plateaus based on Eq. (11) in Ref. [18] have been added for all curves as a guide to the reader's eye (solid lines in Fig. 12). The effects of composition and structure are evident in the reaction-controlled regime, where the crack velocity curves shift to lower energy release rates with increasing OMCTS flow rate (increasing C content), indicating a reduced resistance to fracture with decreasing network connectivity.

The subcritical measurements in DI water show energy release rates that are significantly reduced as compared to the measurements in a dry environment, suggesting that OSG films are very susceptible to stress-corrosion cracking. In fact, the detrimental effect of water is so strong that the

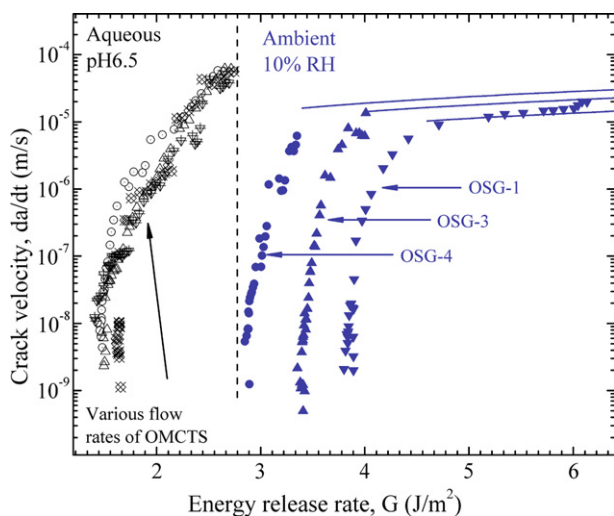


Fig. 12. Subcritical fracture curves in both dry ambient and aqueous environment for the OSG/silicon nitride interface.

adhesion enhancement due to the increased network connectivity and interfacial densification is greatly diminished, and is entirely lost in the experimental scatter. To avoid adhesion degradation, it is critical to minimize exposure of OSG films to water during or after the integrated circuits fabrication process [43].

4. Conclusions

This study has shown that the mechanical properties of OSG films depend sensitively on their carbon content and network structure. A small reduction in carbon content leads to increased network connectivity and hence improved mechanical behavior. Mechanical behavior can also be improved by UV irradiation of the films, without a significant change in dielectric constant. Structure analysis reveals that UV irradiation severs weak terminal bonds and creates networking bonds. The UV cure also provides the energy for local bond rearrangement where large angle Si—O—Si bonds are converted to more stable small-angle bonds with larger bond energy.

Both the mean connectivity number and the network bond density correlate well with the stiffness and the hardness of the films over a limited range of process parameters. The weighted network bond density, on the other hand, works for a broad range of conditions and even captures the effect of the UV cure. The cohesive energy of OSG films scales linearly with the weighted networking bond density of the films. The adhesion energy between silicon nitride and OSG as measured by four-point bending is significantly larger than the cohesive energy of the OSG films. The difference between the adhesive and cohesive energies can be attributed to the densification of the surface of the OSG films during the deposition of the silicon nitride as well as to crack-tip shielding. Subcritical adhesion measurements, however, show that this enhancement vanishes when the films are exposed to water.

Acknowledgments

The authors acknowledge funding from the Semiconductor Research Corporation (2005-KC-1292.011, 2005-KJ-1339.001) and the School of Engineering and Applied Sciences at Harvard University. The OSG film stacks were provided by Texas Instruments Incorporated. The authors thank Dr. Nancy Ota for help with the nanoindentation measurements.

References

- [1] International technology roadmap for semiconductors, 2006 Update.
- [2] Kim JY, Hwang MS, Kim YH, Kim HJ, Lee Y. J Appl Phys 2001;90:2469.
- [3] Lin Y, Tsui TY, Vlassak JJ. J Electrochem Soc 2006;153.
- [4] Tsui TY, McKerrow AJ, Vlassak JJ. J Mater Res 2005;20:2266.
- [5] O'Neill ML, Haas MK, Peterson BK, Vrtis RN, Weigel SJ, Wu D, et al. Mater Res Soc Symp P 2006;914:F01.

- [6] Vlassak JJ, Nix WD. *J Mater Res* 1992;7:3242.
- [7] Xiang Y, Chen X, Vlassak JJ. *J Mater Res* 2005;20:2360.
- [8] Xiang Y, Chen X, Tsui TY, Jang JI, Vlassak JJ. *J Mater Res* 2006;21:386.
- [9] Oliver WC, Pharr GM. *J Mater Res* 2004;19:3.
- [10] Oliver WC, Pharr GM. *J Mater Res* 1992;7:1564.
- [11] King RB. *Int J Solids Struct* 1987;23:1657.
- [12] Kanninen MF. *Int J Fracture* 1973;9:83.
- [13] Charalambides PG, Cao HC, Lund J, Evans AG. *Mech Mater* 1990;8:269.
- [14] Charalambides PG, Lund J, Evans AG, McMeeking RM. *J Appl Mech* 1989;56:77.
- [15] Hughey MP, Morris DJ, Cook RF, Bozeman SP, Kelly BL, Chakravarty SLN, et al. *Eng Fract Mech* 2004;71:245.
- [16] Lin Y, Vlassak JJ, Tsui TY, McKerrow AJ. *Mater Res Soc Symp Proc* 2003;766:171.
- [17] Lin Y, Vlassak JJ, Tsui TY, McKerrow AJ. *Mater Res Soc Symp Proc* 2004;795:93.
- [18] Vlassak JJ, Lin Y, Tsui TY. *Mater Sci Eng A-Struct Mater Prop Microstruct Process* 2005;391:159.
- [19] Grill A, Neumayer DA. *J Appl Phys* 2003;94:6697.
- [20] Phillips JC. *J Non-Cryst Solids* 1979;34:153.
- [21] Dohler GH, Dandolo R, Bilz H. *J Non-Cryst Solids* 1980;42:87.
- [22] Thorpe MF. *J Non-Cryst Solids* 1983;57:355.
- [23] He H, Thorpe MF. *Phys Rev Lett* 1985;54:2107.
- [24] Feng XW, Bresser WJ, Zhang M, Goodman B, Boolchand P. *J Non-Cryst Solids* 1997;222:137.
- [25] Phillips JC. *Solid State Commun* 1983;47:203.
- [26] Kerner R, Phillips JC. *Solid State Commun* 2000;117:47.
- [27] Chen X, Vlassak JJ. *J Mater Res* 2001;16:2974.
- [28] Carlotti G, Cherault N, Casanova N, Goldberg C, Socino G. *Thin Solid Films* 2005;493:175.
- [29] Ross AD, Gleason KK. *J Appl Phys* 2005:97.
- [30] Iacopi F, Travaly Y, Eyckens B, Waldfried C, Abell T, Guyer EP, et al. *J Appl Phys* 2006:99.
- [31] Burkey DD, Gleason KK. *J Appl Phys* 2003;93:5143.
- [32] Guyer EP, Patz M, Dauskardt RH. *J Mater Res* 2006;21:882.
- [33] Toivola Y, Thurn J, Cook RF. *J Electrochem Soc* 2002;149:F9.
- [34] Kim S, Toivola Y, Cook RF, Char K, Chu SH, Lee JK, et al. *J Electrochem Soc* 2004;151:F37.
- [35] Toivola Y, Kim S, Cook RF, Char K, Lee JK, Yoon DY, et al. *J Electrochem Soc* 2004;151:F45.
- [36] Boolchand P, Zhang M, Goodman B. *Phys Rev B* 1996;53:11488.
- [37] *Handbook of Chemistry and Physics*. Boca Raton, Florida: CRC Press LLC; 2001.
- [38] Kim YK, Lee HS, Yeom HW, Ryoo DY, Huh SB, Lee JG. *Phys Rev B* 2004:70.
- [39] Oshima M, Toyoda S, Okabayashi J, Kumigashira H, Ono K, Niwa M, et al. *J Vac Sci Technol A* 2004;22:176.
- [40] Li HF, Dimitrijevic S, Sweatman D, Harrison HB, Tanner P, Feil B. *J Appl Phys* 1999;86:4316.
- [41] Wiederhorn SM, Diness AM, Heuer AH. *J Am Ceram Soc* 1974;57:336.
- [42] Evans AG, Hutchinson JW. *Acta Metall* 1989;37:909.
- [43] Lin Y, Tsui TY, Vlassak JJ. *Acta Mater* 2007;55:2455.